INTERNATIONAL JOURNAL FOR NUMERICAL METHODS IN FLUIDS
Int. J. Numer. Meth. Fluids 2004; **45**:605–623 (DOI: 10.1002/fld.709)

A triangular spectral/*hp* discontinuous Galerkin method for modelling 2D shallow water equations

C. Eskilsson[1,2] and S. J. Sherwin[2,*,†]

[1] *Water Environment Transport, Chalmers University of Technology, Göteborg SE-412 96, Sweden*
[2] *Department of Aeronautics, Imperial College London, London SW7 2AZ, U.K.*

SUMMARY

We present a spectral/*hp* element discontinuous Galerkin model for simulating shallow water flows on unstructured triangular meshes. The model uses an orthogonal modal expansion basis of arbitrary order for the spatial discretization and a third-order Runge–Kutta scheme to advance in time. The local elements are coupled together by numerical fluxes, evaluated using the HLLC Riemann solver. We apply the model to test cases involving smooth flows and demonstrate the exponentially fast convergence with regard to polynomial order. We also illustrate that even for results of 'engineering accuracy' the computational efficiency increases with increasing order of the model and time of integration. The model is found to be robust in the presence of shocks where Gibbs oscillations can be suppressed by slope limiting. Copyright © 2004 John Wiley & Sons, Ltd.

KEY WORDS: discontinuous Galerkin method; spectral/*hp* discretization; shallow water equations

1. INTRODUCTION

In many hydrodynamic applications of interest to hydraulic, coastal and ocean engineering the characteristic length scale of the problem is large compared to the vertical scale. In this case, the flow can be regarded as uniform in depth and approximated by the shallow water equations (SWE). The SWE are a two-dimensional system of non-linear partial differential equations of hyperbolic type.

The body of literature on numerical modelling of the SWE is vast and covers all types of numerical methods. The models used in coastal and hydraulic engineering are generally of low-order—possibly with shock-capturing—e.g. References [1–3], while in oceanographic and atmospheric sciences the numerical algorithms are predominantly of high-order, e.g. the quadrilateral nodal spectral element models of Ma [4] and Iskandarani *et al.* [5]. High-order Galerkin finite element (FE) methods have the appealing property of combining the geometrical flexibility of *h*-type finite element methods with the high accuracy of the *p*-type spectral methods. The above-mentioned spectral element models have been shown to exhibit exponentially fast convergence for smooth waves on staggered [5] and unstaggered [4]

*Correspondence to: Spencer J. Sherwin, Department of Aeronautics, Imperial College London, Prince Consort Road, London SW7 2AZ, U.K.
†E-mail: s.sherwin@imperial.ac.uk

Published online 8 April 2004
Received 24 February 2003
Revised 15 December 2003

meshes. In these approaches, a nodal quadrilateral spectral/*hp* element methods was applied using a Lagrange polynomial basis through the Gauss–Lobatto–Legendre quadrature points. This method has a discrete diagonal mass matrix, if a slight under integration is applied, which is significant for the efficiency of the method. Within triangular subdomains modal or hierarchical basis are often applied. However, for modal spectral/*hp* element discretizations using a classical Galerkin formulation the mass matrix is not diagonal which severely limits the efficiency of the implementation. Nevertheless, as demonstrated in this paper, this problem can be overcome by using a discontinuous Galerkin formulation.

In this study, we therefore will solve the SWE using a modal triangular spectral/*hp* discontinuous Galerkin (DG) method following the Runge–Kutta DG method developed by Cockburn and Shu and co-workers, e.g. References [6–8]. The key feature of the DG method is that solutions are allowed to be discontinuous over elemental boundaries, while the elements are coupled using numerical fluxes similar to the finite volume technique. Of course, in the presence of discontinuities such as shocks, Gibbs oscillations arise if the polynomial expansions employed are linear or higher, but—in contrast to classical continuous Galerkin methods—the oscillations generally do not appear to pollute the whole solution or cause the solution to 'blow-up'. Further, the Gibbs oscillations can be suppressed by slope limiting [9, 7, 10]. In addition to allowing shocks to form and propagate in the domain, the DG method gives stable solutions for equal-order approximations [11] and staggered meshes or mixed approximations are therefore unnecessary.

The DG method has been applied to the SWE for simulating flows involving shocks, such as dam-break flows and oblique hydraulic jumps [12–14]. These three studies used essentially low-order approximation on unstructured triangular meshes and suppressed any Gibbs oscillations by applying limiting procedures. Previous high-order DG SWE models are the nodal spectral element methods of Dupont [15] and Giraldo *et al.* [16]. Dupont used triangular elements in which the expansion basis was made up from a product of 1D Legendre polynomials with triangular truncation. Giraldo *et al.* solved the SWE on the sphere using curvilinear quadrilaterals. The elemental solution was approximated by a nodal Lagrange polynomial, constructed from a tensor product of 1D Legendre cardinal functions, giving a diagonal mass matrix if under integration was performed. The exponential convergence of the two models were confirmed by numerical tests. In addition, Giraldo *et al.* investigated the effect of solving the equations in divergence form rather than in Green's form. Although it was shown that the Green's formulation provided more accurate solutions, the difference was found negligible for the test cases considered.

The paper is organized as follows. In Section 2, we outline the governing equations. The numerical model is presented in Section 3, and applied to several test cases in Section 4. Finally, in Section 5 we summarize the study and present our conclusions.

2. GOVERNING EQUATIONS

The 2D SWE, expressed in terms of conservative variables, is written in conservation form as

$$\frac{\partial \mathbf{U}}{\partial t} + \nabla \cdot \mathbf{F}(\mathbf{U}) = \mathbf{S}(\mathbf{U}) \tag{1}$$

where $\mathbf{F}(\mathbf{U}) = [\mathbf{E}(\mathbf{U}), \mathbf{G}(\mathbf{U})]^{\mathrm{T}}$ and

$$\mathbf{U} = \begin{bmatrix} H \\ uH \\ vH \end{bmatrix}, \quad \mathbf{E} = \begin{bmatrix} uH \\ u^2H + gH^2/2 \\ uvH \end{bmatrix}, \quad \mathbf{G} = \begin{bmatrix} vH \\ uvH \\ v^2H + gH^2/2 \end{bmatrix} \tag{2}$$

Here $H(x, y, t) = \zeta(x, y, t) + d(x, y)$ is the total water depth, $d(x, y)$ is the still water depth and $\zeta(x, y, t)$ is the free surface elevation; $u(x, y, t)$ and $v(x, y, t)$ are the depth-averaged velocities in the x- and y-direction, respectively, and g is the acceleration due to gravity. The source term $\mathbf{S}$ accounts for forcing due to friction, bed slopes and Coriolis effects and is defined as

$$\mathbf{S} = \begin{bmatrix} 0 \\ gH(S_{0_x} - S_{f_x}) + fv \\ gH(S_{0_y} - S_{f_y}) - fu \end{bmatrix} \tag{3}$$

where S_{0_x} and S_{0_y} are the bed slopes in the x- and y-direction, respectively. The Coriolis parameter f is given by the β-plane approximation, i.e. $f = f_0 + \beta y$. The friction losses are estimated by the Manning law

$$S_{f_x} = \frac{uM^2\sqrt{u^2 + v^2}}{H^{4/3}}, \qquad S_{f_y} = \frac{vM^2\sqrt{u^2 + v^2}}{H^{4/3}} \tag{4}$$

where M is the Manning number.

Considering the homogeneous equations, the SWE can be quasi-linearized as

$$\frac{\partial \mathbf{U}}{\partial t} + \frac{\partial \mathbf{E}}{\partial \mathbf{U}} \frac{\partial \mathbf{U}}{\partial x} + \frac{\partial \mathbf{G}}{\partial \mathbf{U}} \frac{\partial \mathbf{U}}{\partial y} = \mathbf{0} \tag{5}$$

where the Jacobians of the flux functions can be evaluated as

$$\frac{\partial \mathbf{E}(\mathbf{U})}{\partial \mathbf{U}} = \begin{bmatrix} 0 & 1 & 0 \\ c^2 - u^2 & 2u & 0 \\ -uv & v & u \end{bmatrix}, \quad \frac{\partial \mathbf{G}(\mathbf{U})}{\partial \mathbf{U}} = \begin{bmatrix} 0 & 0 & 1 \\ -uv & v & u \\ c^2 - v^2 & 0 & 2v \end{bmatrix} \tag{6}$$

in which $c = \sqrt{gH}$ is the wave speed. Defining an arbitrary unit vector $\mathbf{s} = [s_{\mathrm{x}}, s_{\mathrm{y}}]^{\mathrm{T}}$, we obtain the following Jacobian matrix:

$$\frac{\partial(\mathbf{F}(\mathbf{U}) \cdot \mathbf{s})}{\partial \mathbf{U}} = \begin{bmatrix} 0 & s_{\mathrm{x}} & s_{\mathrm{y}} \\ (c^2 - u^2)s_{\mathrm{x}} - uvs_{\mathrm{y}} & 2us_{\mathrm{x}} + vs_{\mathrm{y}} & us_{\mathrm{y}} \\ -uvs_{\mathrm{x}} + (c^2 - v^2)s_{\mathrm{y}} & vs_{\mathrm{x}} & us_{\mathrm{x}} + 2vs_{\mathrm{y}} \end{bmatrix} \tag{7}$$

with eigenvalues

$$\lambda_1 = us_{\mathrm{x}} + vs_{\mathrm{y}} - c, \quad \lambda_2 = us_{\mathrm{x}} + vs_{\mathrm{y}}, \quad \lambda_3 = us_{\mathrm{x}} + vs_{\mathrm{y}} + c \tag{8}$$

The matrices of corresponding right ($\mathbf{R}=[\mathbf{r}_1,\mathbf{r}_2,\mathbf{r}_3]$) and left ($\mathbf{L}=[\mathbf{l}_1,\mathbf{l}_2,\mathbf{l}_3]^{\mathrm{T}}$) eigenvectors are

$$\mathbf{R}=\begin{bmatrix} 1 & 0 & 1 \\ u-cs_{\mathrm{x}} & s_{\mathrm{y}} & u+cs_{\mathrm{x}} \\ v-cs_{\mathrm{y}} & -s_{\mathrm{x}} & v+cs_{\mathrm{y}} \end{bmatrix} \tag{9}$$

and

$$\mathbf{L}=\frac{1}{2c}\begin{bmatrix} us_{\mathrm{x}}+vs_{\mathrm{y}}+c & -s_{\mathrm{x}} & -s_{\mathrm{y}} \\ 2c(-us_{\mathrm{y}}+vs_{\mathrm{x}}) & 2cs_{\mathrm{y}} & -2cs_{\mathrm{x}} \\ -us_{\mathrm{x}}-vs_{\mathrm{y}}+c & s_{\mathrm{x}} & s_{\mathrm{y}} \end{bmatrix} \tag{10}$$

respectively.

3. DISCONTINUOUS GALERKIN MODEL

3.1. Galerkin formulation

The computational domain Ω is divided into N non-overlapping triangular elements denoted by $\mathscr{T}_e$ of characteristic size h_e and with boundary $\partial\mathscr{T}_e$ such that

$$\Omega = \bigcup_{e=1}^{N} \mathscr{T}_e \tag{11}$$

Multiplying Equation (1) by a smooth function $\mathbf{q}(\mathbf{x})$ and integrating over the element $\mathscr{T}_e$ we obtain

$$\int_{\mathscr{T}_e} \frac{\partial \mathbf{U}_i}{\partial t}\,\mathbf{q}_i\,\mathrm{d}\mathbf{x}+\int_{\mathscr{T}_e}(\nabla\cdot\mathbf{F}(\mathbf{U}))_i\,\mathbf{q}_i\,\mathrm{d}\mathbf{x}=\int_{\mathscr{T}_e}\mathbf{S}(\mathbf{U})_i\,\mathbf{q}_i\,\mathrm{d}\mathbf{x} \tag{12}$$

Integrating the second term in Equation (12) by parts gives

$$\int_{\mathscr{T}_e} \frac{\partial \mathbf{U}_i}{\partial t}\,\mathbf{q}_i\,\mathrm{d}\mathbf{x}-\int_{\mathscr{T}_e}(\mathbf{F}(\mathbf{U})\cdot\nabla)_i\,\mathbf{q}_i\,\mathrm{d}\mathbf{x}+\int_{\partial\mathscr{T}_e}(\mathbf{F}(\mathbf{U})\cdot\mathbf{n})_i\,\mathbf{q}_i\,\mathrm{d}s=\int_{\mathscr{T}_e}\mathbf{S}(\mathbf{U})_i\,\mathbf{q}_i\,\mathrm{d}\mathbf{x} \tag{13}$$

where $\mathbf{n}=(n_{\mathrm{x}},n_{\mathrm{y}})^{\mathrm{T}}$ is the outward unit normal to $\mathscr{T}_e$. The discrete Galerkin approximation is obtained by replacing $\mathbf{q}$ with a test function $\mathbf{q}_\delta\in\mathscr{V}_\delta$ as well as approximating the exact solution $\mathbf{U}$ with $\mathbf{U}_\delta\in\mathscr{V}_\delta$, where the discrete space $\mathscr{V}_\delta$ is defined as

$$\mathscr{V}_\delta=\{q_\delta\in L^2(\Omega): q_\delta|_{\mathscr{T}_e}\in\mathscr{P}^P(\mathscr{T}_e),\ \forall\mathscr{T}_e\} \tag{14}$$

Here $\mathscr{P}^P(\mathscr{T}_e)$ is the space of polynomials of degree at most P in the element $\mathscr{T}_e$. To allow information to propagate between elements, as the elements are discontinuous at the elemental boundaries, we replace the boundary flux $\mathbf{F}(\mathbf{U})$ that appears in the third term of Equation (13) with an upwind numerical flux, to be discussed later. We denote the numerical

flux with $\hat{\mathbf{F}}(\mathbf{U})$. Thus, we write the DG formulation (after analytically integrating by parts once more to obtain the divergence form): Find $\mathbf{U}_\delta \in \mathscr{V}_\delta$ such that $\forall \mathbf{q}_\delta \in \mathscr{V}_\delta$

$$\int_{\mathscr{T}_e} \frac{\partial \mathbf{U}_{\delta i}}{\partial t} \mathbf{q}_{\delta i} \, \mathrm{d}\mathbf{x} + \int_{\mathscr{T}_e} (\nabla \cdot \mathbf{F}(\mathbf{U}_\delta))_i \mathbf{q}_{\delta i} \, \mathrm{d}\mathbf{x} + \int_{\partial \mathscr{T}_e} ((\hat{\mathbf{F}}(\mathbf{U}_\delta) - \mathbf{F}(\mathbf{U}_\delta)) \cdot \mathbf{n})_i \mathbf{q}_{\delta i} \, \mathrm{d}s = \int_{\mathscr{T}_e} \mathbf{S}(\mathbf{U}_\delta)_i \mathbf{q}_{\delta i} \, \mathrm{d}\mathbf{x} \tag{15}$$

For computational convenience we prefer the divergence form since it involves inner products of the same forms as classical continuous Galerkin schemes.

3.2. *Expansion basis and collapsed co-ordinate system*

We use the hierarchical and orthogonal basis functions proposed independently by Proriol [17], Koornwinder [18] and Dubiner [19], which is a warped product of a one-dimensional tensor and a two-dimensional tensor. We start by introducing the one-to-one mapping from global Cartesian co-ordinates (x, y) to local Cartesian co-ordinates (ξ_1, ξ_2) denoted as

$$(x, y) = \chi_e(\xi_1, \xi_2) \tag{16}$$

The mapping of the triangular domain $\mathscr{T}_e$ into the standard triangle $\mathscr{T}_{\mathrm{st}}$ is given by $\chi_e^{-1}(\mathscr{T}_e) = \mathscr{T}_{\mathrm{st}}$, where the standard triangle is defined by

$$\mathscr{T}_{\mathrm{st}} = \{(\xi_1, \xi_2) | -1 \leqslant \xi_1, \xi_2; \xi_1 + \xi_2 \leqslant 0\} \tag{17}$$

As the standard triangular domain is not independently bounded by the co-ordinates (ξ_1, ξ_2), we introduce the so-called collapsed co-ordinate system (η_1, η_2) [20]. The transformation from $(\xi_1, \xi_2) \to (\eta_1, \eta_2)$ is given by

$$\eta_1 = 2 \frac{(1 + \xi_1)}{(1 - \xi_2)} - 1, \quad \eta_2 = \xi_2 \tag{18}$$

The standard triangle can now be defined in terms of collapsed co-ordinates as

$$\bar{\mathscr{T}}_{\mathrm{st}} = \{(\eta_1, \eta_2) | -1 \leqslant \eta_1, \eta_2 \leqslant 1\} \tag{19}$$

which has independent limits. The transformation to collapsed co-ordinate system can be interpreted as a mapping to a standard quadrilateral region (see Figure 1). The orthogonal expansion modes ϕ_{pq} are defined using warped tensors

$$\phi_{pq}(\xi_1, \xi_2) = \tilde{\psi}_p^a(\eta_1) \tilde{\psi}_{pq}^b(\eta_2) \tag{20}$$

If $P_p^{\alpha,\beta}(z)$ denotes the pth-order Jacobi polynomial, the principal functions $\tilde{\psi}_i^a(z)$ and $\tilde{\psi}_{ij}^b(z)$ are defined as

$$\tilde{\psi}_i^a(z) = P_i^{0,0}(z), \quad \tilde{\psi}_{ij}^b(z) = \left(\frac{1 - z}{2}\right)^i P_j^{2i+1,0}(z) \tag{21}$$

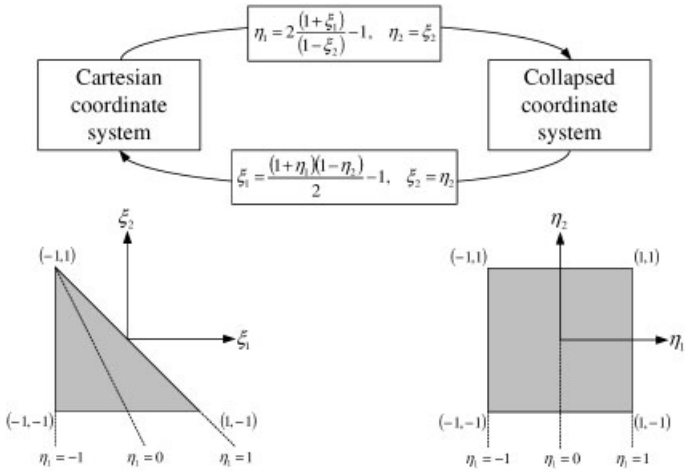

Figure 1. The standard triangle in Cartesian and collapsed co-ordinates.

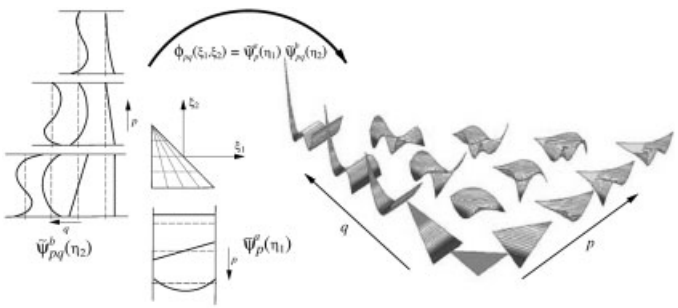

Figure 2. Construction of the p-type expansion basis.

The construction of the two-dimensional expansion basis is illustrated in Figure 2. In addition to giving rise to an orthogonal mass matrix, the use of the collapsed co-ordinate system means that integrals over the domain $\mathscr{T}_e$ can be evaluated as the product of two one-dimensional integrals. We can therefore use Gauss–Lobatto quadrature in the ξ_1-direction and Gauss–Radau quadrature in the ξ_2-direction, in order to avoid incorporating any information from the geometrically singular vertex ($\xi_1 = -1$, $\xi_2 = 1$). Note that even though there are two transformations, $(x, y) \to (\xi_1, \xi_2)$ and $(\xi_1, \xi_2) \to (\eta_1, \eta_2)$, the second transformation can be incorporated in the quadrature weights and therefore does not have to be computed explicitly.

Finally, we write the approximate solution within an element $\mathbf{U}_\delta$ as

$$\mathbf{U}_\delta(\mathbf{x}, t) = \sum_{p=0}^{P} \sum_{q=0}^{P} \tilde{\mathbf{U}}_{pq}(t)\phi_{pq}(\xi_1, \xi_2), \quad \mathbf{x} \in \mathscr{T}_e \tag{22}$$

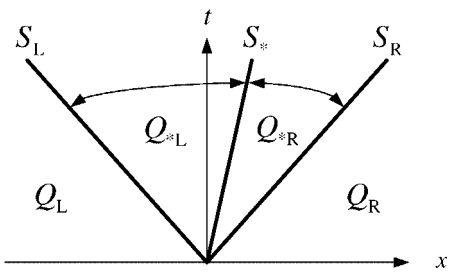

Figure 3. Three wave structure of the HLLC approximate Riemann solver.

where $\tilde{\mathbf{U}}_{pq}(t)$ contains the local degrees of freedom of expansion coefficients and the trial functions $\phi_{pq}(\xi_1, \xi_2)$ (and also the test functions) are described by Equation (20).

3.3. Numerical flux

As mentioned above integrals over the domain $\mathcal{T}_e$ are evaluated using Gauss–Lobatto and Gauss–Radau quadrature rules. However, using the Gauss–Lobatto or Gauss–Radau quadrature when estimating the surface integral would mean having to estimate a 2D flux at the endpoints (corresponding to the vertices). Hence, it is advantageous to use Gauss quadrature points as the endpoints are not included. Computing the flux at a Gauss point on the edge corresponds to solving a 1D Riemann problem in the normal direction to the edge.

In the context of DG SWE models, previously both the Roe and HLL approximate solvers have been successfully applied [12, 14], with equivalent results [12]. Alternatively, the numerical flux can be evaluated using the simpler but more dissipative Lax–Friedrich flux [13, 16]. In the case of smooth flows even straightforward averaging have been reported to work [15].

For high-order DG methods the most widely used numerical flux is the Lax–Friedrich flux, as the importance of the choice of flux appears to decrease with increasing expansion order [8]. However, in the case of shocks the application of the generalized slope limiter will lower the approximation within the element to linear and so the Lax–Friedrich flux might prove too dissipative. In this study, we have therefore adopted the HLLC approximate Riemann solver in conjunction with the two-rarefaction assumption [3].

Introducing the rotation matrix and its inverse

$$\mathbf{T} = \begin{bmatrix} 1 & 0 & 0 \\ 0 & n_x & n_y \\ 0 & -n_y & n_x \end{bmatrix}, \quad \mathbf{T}^{-1} = \begin{bmatrix} 1 & 0 & 0 \\ 0 & n_x & -n_y \\ 0 & n_y & n_x \end{bmatrix} \tag{23}$$

we subsequently define $\mathbf{Q} = \mathbf{T}\mathbf{U}_\delta = [H, H\bar{u}, H\bar{v}]^T$; where $\bar{u}$ and $\bar{v}$ are the velocities in the direction normal and tangential to the edge, respectively. The 1D flux at a Gauss point can be written

$$\hat{\mathbf{F}}(\mathbf{U}_\delta) \cdot \mathbf{n} = \mathbf{T}^{-1}\hat{\mathbf{E}}(\mathbf{Q}) \tag{24}$$

The HLLC solver [3] is based on three wave speed estimates as illustrated in Figure 3, where the subscripts L and R stand for the left- and right-hand side of the element boundary. We

estimate the wave speeds as [3]

$$S_{\mathrm{L}} = \bar{u}_{\mathrm{L}} - \sqrt{gH_{\mathrm{L}}}s_{\mathrm{L}} \tag{25a}$$

$$S_{\mathrm{R}} = \bar{u}_{\mathrm{R}} + \sqrt{gH_{\mathrm{R}}}s_{\mathrm{R}} \tag{25b}$$

$$S_* = \frac{S_{\mathrm{L}}H_{\mathrm{R}}(\bar{u}_{\mathrm{R}} - S_{\mathrm{R}}) - S_{\mathrm{R}}H_{\mathrm{L}}(\bar{u}_{\mathrm{L}} - S_{\mathrm{L}})}{H_{\mathrm{R}}(\bar{u}_{\mathrm{R}} - S_{\mathrm{R}}) - H_{\mathrm{L}}(\bar{u}_{\mathrm{L}} - S_{\mathrm{L}})} \tag{25c}$$

where

$$s_{(\mathrm{L,R})} = \begin{cases} \sqrt{(H_*^2 + H_*H_{(\mathrm{L,R})})/(2H_{(\mathrm{L,R})}^2)} & \text{if } H_* > H_{(\mathrm{L,R})} \\ 1 & \text{if } H_* \leqslant H_{(\mathrm{L,R})} \end{cases} \tag{26}$$

and in which H_* is given by the two-rarefaction Riemann solver:

$$H_* = \frac{1}{g}\left(\frac{1}{2}(\sqrt{gH_{\mathrm{L}}} + \sqrt{gH_{\mathrm{R}}}) + \frac{1}{4}(\bar{u}_{\mathrm{L}} - \bar{u}_{\mathrm{R}})\right)^2 \tag{27}$$

After the wave speeds have been computed the HLLC flux is given by

$$\hat{\mathbf{E}}(\mathbf{Q}) = \begin{cases} \mathbf{E}(\mathbf{Q}_{\mathrm{L}}) & \text{if } S_{\mathrm{L}} \geqslant 0 \\ \mathbf{E}(\mathbf{Q}_{\mathrm{L}}) + S_{\mathrm{L}}(\mathbf{Q}_{*\mathrm{L}} - \mathbf{Q}_{\mathrm{L}}) & \text{if } S_{\mathrm{L}} \leqslant 0 \leqslant S_* \\ \mathbf{E}(\mathbf{Q}_{\mathrm{R}}) + S_{\mathrm{R}}(\mathbf{Q}_{*\mathrm{R}} - \mathbf{Q}_{\mathrm{R}}) & \text{if } S_* \leqslant 0 \leqslant S_{\mathrm{R}} \\ \mathbf{E}(\mathbf{Q}_{\mathrm{R}}) & \text{if } S_{\mathrm{R}} \leqslant 0 \end{cases} \tag{28}$$

where $\mathbf{Q}_{*\mathrm{L}}$ and $\mathbf{Q}_{*\mathrm{R}}$ are obtained from

$$\mathbf{Q}_{*(\mathrm{L,R})} = H_{(\mathrm{L,R})}\left(\frac{S_{(\mathrm{L,R})} - \bar{u}_{(\mathrm{L,R})}}{S_{(\mathrm{L,R})} - S_*}\right)\begin{bmatrix} 1 \\ S_* \\ \bar{v}_{(\mathrm{L,R})} \end{bmatrix} \tag{29}$$

3.4. Boundary conditions

For all element edges aligned on a domain boundary we assign a dummy edge and enforce the boundary conditions via the Riemann solver.

At a wall boundary we assume slip condition: $(u, v) \cdot \mathbf{n} = 0$. This is enforced by setting

$$\zeta_{\mathrm{R}} = \zeta_{\mathrm{L}}, \quad \bar{u}_{\mathrm{R}} = -\bar{u}_{\mathrm{L}}, \quad \bar{v}_{\mathrm{R}} = \bar{v}_{\mathrm{L}} \tag{30}$$

assuming that the local edge is the left state and the dummy edge is the right state, respectively. At inflow boundaries, we set the values at the dummy edge to the *a priori* known values and so the condition is enforced weakly through the characteristic variables. In the case where reflected outgoing waves appear at the inflow boundary, we apply the non-reflecting flux

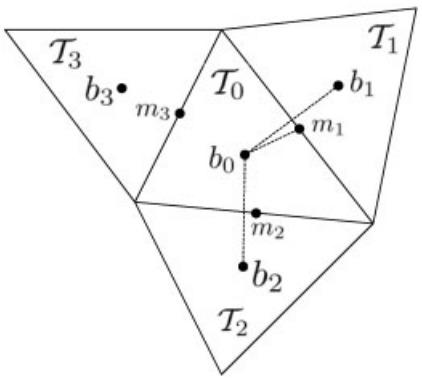

Figure 4. Notation for limiting.

function [21] which is found to work satisfactorily for higher p if the outgoing waves are reasonably normal to the boundary. For outflow boundaries, if the flow can be expected to be reasonably close to the normal direction, the values at the dummy edge is set equal to the undisturbed initial state.

3.5. Time stepping

The time stepping is carried out using the explicit third-order Runge–Kutta scheme described in Reference [6]. Writing the semi-discrete equations as $\partial_t \mathbf{U}_\delta = \mathbf{L}_\delta(\mathbf{U}_\delta)$, advancing from time level n to $n+1$ are computed in three steps:

$$1. \quad \mathbf{U}_\delta^{(1)} = \mathbf{U}_\delta^n + \Delta t \mathbf{L}_\delta(\mathbf{U}_\delta^n) \tag{31a}$$

$$2. \quad \mathbf{U}_\delta^{(2)} = \tfrac{3}{4}\mathbf{U}_\delta^n + \tfrac{1}{4}(\mathbf{U}_\delta^{(1)} + \Delta t \mathbf{L}_\delta(\mathbf{U}_\delta^{(1)})) \tag{31b}$$

$$3. \quad \mathbf{U}_\delta^{n+1} = \tfrac{1}{3}\mathbf{U}_\delta^n + \tfrac{2}{3}(\mathbf{U}_\delta^{(2)} + \Delta t \mathbf{L}_\delta(\mathbf{U}_\delta^{(2)})) \tag{31c}$$

The restriction on the time step is of order $\mathcal{O}(P^{-2})$, since the growth of the eigenvalue of the advection operator is $\mathcal{O}(P^2)$ [20].

3.6. Slope limiting

When simulating shocks we apply the generalized slope limiter, $\Lambda\Pi_h$, of Cockburn and Shu [8] after each Runge–Kutta substep. The $\Lambda\Pi_h$ limiter works on the linear part of the approximation. In order to determine when to limit our solution we compute the jump between elements for the linear part of the approximation. If the jump is larger than a prescribed tolerance the approximation is lowered locally to second-order and the limiter is invoked.

The notation of the limiting is illustrated in Figure 4, where $\mathbf{b}_i$ refer to the barycentres of the triangles $\mathcal{T}_i$, $i=0,1,2,3$. The mid-point of the edges of the element to be limited, $\mathcal{T}_0$, are indicated by $\mathbf{m}_i$, $i=1,2,3$. The non-negative coefficients α_i and β_i depend on $\mathbf{m}_i$

and the geometry, e.g.:

$$\mathbf{m}_1 - \mathbf{b}_0 = \alpha_1(\mathbf{b}_1 - \mathbf{b}_0) + \beta_1(\mathbf{b}_2 - \mathbf{b}_0) \tag{32}$$

and for linear functions, denoted by the subscript 1, we subsequently get

$$\mathbf{A}(\mathbf{m}_1, \mathscr{T}_0) \equiv \mathbf{U}_1(\mathbf{m}_1) - \bar{\mathbf{U}}_{\mathscr{T}_0} = \alpha_1(\bar{\mathbf{U}}_{\mathscr{T}_1} - \bar{\mathbf{U}}_{\mathscr{T}_0}) + \beta_1(\bar{\mathbf{U}}_{\mathscr{T}_2} - \bar{\mathbf{U}}_{\mathscr{T}_0}) \equiv \mathbf{B}(\mathbf{m}_1, \mathscr{T}_0) \tag{33}$$

Here $\bar{\mathbf{U}}_{\mathscr{T}_i}$ is the mean value of $\mathbf{U}_\delta$ in $\mathscr{T}_i$, which for the modal basis adopted in this work is simply equal to $\tilde{\mathbf{U}}_{00}(\mathscr{T}_i)$ (the first modal expansion coefficient).

The limiting is performed on the characteristic fields. Considering the Jacobian

$$\frac{\partial \mathbf{F}(\bar{\mathbf{U}}_{\mathscr{T}_0})}{\partial \mathbf{U}} \cdot \frac{\mathbf{m}_i - \mathbf{b}_0}{|\mathbf{m}_i - \mathbf{b}_0|} \tag{34}$$

and recalling Equations (9)–(10), we obtain the corresponding $\mathbf{R}$ and $\mathbf{L}$ matrices. Left multiplying $\mathbf{A}(\mathbf{m}_i, \mathscr{T}_0)$ and $\mathbf{B}(\mathbf{m}_i, \mathscr{T}_0)$ with $\mathbf{L}$ generates the characteristic fields.

As discussed in Reference [8] limiting consists of computing the quantities

$$\delta_i = \bar{m}(\mathbf{L}\mathbf{A}(\mathbf{m}_i, \mathscr{T}_0), v\mathbf{L}\mathbf{B}(\mathbf{m}_i, \mathscr{T}_0)) \tag{35}$$

where $v > 1$ is an auxiliary parameter (set equal to 2). The modified minmod function, $\bar{m}$, is defined as

$$\bar{m}(a_1, a_2) = \begin{cases} a_1 & \text{if } |a_1| \leqslant M(\Delta x)^2 \\ m(a_1, a_2) & \text{otherwise} \end{cases} \tag{36}$$

in which M is a constant (set equal to 50), Δx is a measure of the element size and m is the standard minmod function

$$m(a_1, a_2) = \begin{cases} s \min(|a_1|, |a_2|) & \text{if } s = \operatorname{sign}(a_1) = \operatorname{sign}(a_2) \\ 0 & \text{otherwise} \end{cases} \tag{37}$$

We then return to the original space by left multiplying δ_i with $\mathbf{R} : \Delta_i = \mathbf{R}\delta_i$. Now, we can write the limited solution in $\mathscr{T}_0$ as

$$\Lambda\Pi_h \mathbf{U}_1 = (\tilde{\mathbf{U}}_{00} + \tilde{\tilde{\mathbf{U}}}_{00})\phi_{00} + \tilde{\tilde{\mathbf{U}}}_{01}\phi_{01} + \tilde{\tilde{\mathbf{U}}}_{10}\phi_{10} \tag{38}$$

where [10]

$$\tilde{\tilde{\mathbf{U}}}_{00} = \tfrac{1}{3}(\Delta_1 + \Delta_2 + \Delta_3) \tag{39a}$$

$$\tilde{\tilde{\mathbf{U}}}_{01} = -\tfrac{1}{3}(2\Delta_1 - \Delta_2 - \Delta_3) \tag{39b}$$

$$\tilde{\tilde{\mathbf{U}}}_{10} = \tfrac{1}{2}(\Delta_2 - \Delta_3) \tag{39c}$$

Clearly $\tilde{\tilde{\mathbf{U}}}_{00}$ must be zero in order to keep the mean of $\mathscr{T}_0$ unchanged. If $\tilde{\tilde{\mathbf{U}}}_{00} \neq 0$ then Δ_i are adjusted as suggested in Reference [8] by calculating

$$\text{pos} = \sum_{i=1}^{3} \max(0, \Delta_i), \quad \text{neg} = \sum_{i=1}^{3} \max(0, -\Delta_i) \tag{40}$$

and

$$\theta^+ = \min\left(1, \frac{\text{neg}}{\text{pos}}\right), \quad \theta^- = \min\left(1, \frac{\text{pos}}{\text{neg}}\right) \tag{41}$$

We then compute

$$\tilde{\Delta}_i = \theta^+ \max(0, \Delta_i) - \theta^- \max(0, -\Delta_i) \tag{42}$$

and employ $\tilde{\Delta}_i$ instead of Δ_i in Equations (39a)–(39c).

4. COMPUTATIONAL EXAMPLES

4.1. Standing wave

We demonstrate the exponential convergence of the model by considering the simple case of a linear standing wave in a rectangular frictionless basin, with the analytical solution:

$$H(x, y, t) = d + a \cos(kx) \cos(\omega t) \tag{43a}$$

$$u(x, y, t) = a \frac{\omega}{kd} \sin(kx) \sin(\omega t) \tag{43b}$$

$$v(x, y, t) = 0 \tag{43c}$$

where a is the amplitude, k the wave number and ω the frequency such that $w^2 = gdk^2$. The dimensions of the basin are 200×100 m and the still water depth is set to $d = 10$ m. We compute one wave period for a standing wave of wavelength $L = 400$ m with $a = 0.2$ m, using the linearized SWE with the Coriolis parameter set to zero. The time step is chosen sufficiently small so temporal error is negligible compared to spatial error. In Table I, we present the error and order of accuracy for in the L^2 and L^∞ norms. It is seen that the convergence—when in the asymptotic range—is optimal and of order $\mathcal{O}(h^{P+1})$ in both the L^2 and L^∞ norms for both odd and even P. Thus, in the case of p-type refinement we obtain exponentially fast convergence, as illustrated in Figure 5.

4.2. Equatorial Kelvin and Rossby waves

Here we solve the SWE, including Coriolis forces, in non-dimensional variables (denoted with asterisks):

$$\mathbf{x} = \frac{r}{E^{1/4}} \mathbf{x}^*, \quad t = \frac{E^{1/4}}{2\Omega} t^*, \quad \zeta = d_0 \zeta^*, \quad (u, v) = \frac{1}{\sqrt{g d_0}} (u^*, v^*), \quad f = \frac{2\Omega}{E^{1/4}} y^* \tag{44}$$

Table I. Error and order of convergence for the H-component.

		$N=16$	$N=64$		$N=256$	
Norm	P	Error	Error	Order	Error	Order
L^2	1	5.9368E−01	1.1036E−01	2.43	2.4301E−02	2.18
	2	2.3578E−02	2.9446E−03	3.00	3.6933E−04	3.00
	3	1.1690E−03	7.2890E−05	4.00	4.5704E−06	4.00
	4	4.5379E−05	1.4247E−06	4.99	4.4809E−08	4.99
L^∞	1	1.2106E−02	3.8632E−03	1.65	1.0287E−03	1.91
	2	1.5059E−03	2.1294E−04	2.82	2.5690E−05	3.05
	3	9.8556E−05	6.7661E−06	3.86	4.3254E−07	3.97
	4	5.0395E−06	1.7785E−07	4.82	5.4439E−09	5.03

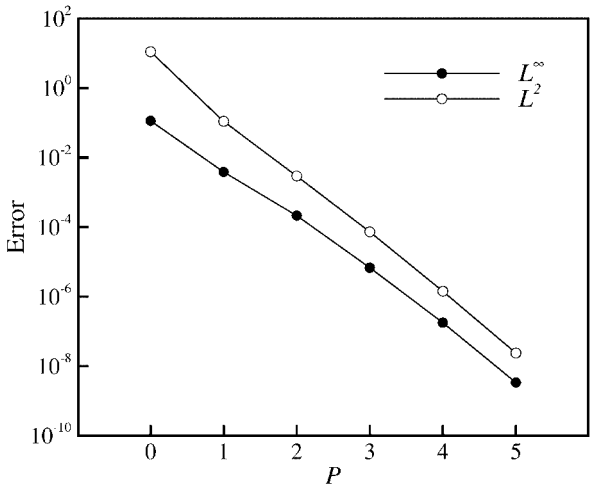

Figure 5. Exponential convergence in the case of p-type refinement ($N=64$).

where $E=4\,\Omega^2 r^2 (g d_0)^{-1}$ is the Lamb parameter, r is the radius of the earth, $\Omega = 2\pi\ \text{day}^{-1}$ is the angular frequency of the earth's rotation and d_0 is the equivalent depth for a reduced gravity model. Using an equivalent depth of 0.40 m, the length scale becomes 295 km and the time scale 1.71 days [22]. For convenience we drop the asterisks for the rest of this section.

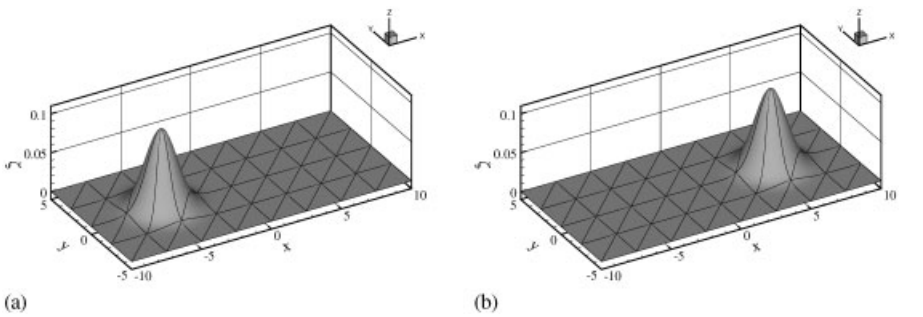

Figure 6. Propagation of an equatorial Kelvin wave (64 elements of order 14): (a) Initial condition and (b) at $t = 10$.

First we use the linearized SWE to simulate a linear equatorial Kelvin wave, with the analytic solution:

$$H(x, y, t) = 1 + \exp\left(-\frac{y^2}{2}\right) \exp\left(-\frac{(x + 5 - t)^2}{2}\right) \tag{45a}$$

$$u(x, y, t) = \exp\left(-\frac{y^2}{2}\right) \exp\left(-\frac{(x + 5 - t)^2}{2}\right) \tag{45b}$$

$$v(x, y, t) = 0 \tag{45c}$$

The equatorial Kelvin wave propagates eastward in a rectangular basin of size 20×10 non-dimensional units with constant depth and semi-periodic boundaries. Setting the friction to zero, the Kelvin wave propagates unchanged (see Figure 6). Integrating for 10 and 100 time units, the CPU times for obtaining an 'engineering accuracy' of 10% and a 'scientific accuracy' of 1% relative error—using different polynomial orders and time steps—are presented in Table II. Note that when obtaining the values presented in Table II, for simplicity, we have used structured uniform triangular meshes. Also, note that for these large errors we are usually not in the asymptotic range of convergence. Nevertheless, from Table II it is evident that the model becomes increasingly efficient with increasing order in the limit of long-time integration.

Secondly, we consider the case of a westward travelling solitary Rossby wave using the non-linear SWE. The zeroth-order initial conditions are given by [22]

$$H(x, y, 0) = 1 + \Gamma(x)\left(\frac{3 + 6y^2}{4}\right) \exp\left(-\frac{y^2}{2}\right) \tag{46a}$$

$$u(x, y, 0) = \Gamma(x)\left(\frac{-9 + 6y^2}{4}\right) \exp\left(-\frac{y^2}{2}\right) \tag{46b}$$

$$v(x, y, 0) = \frac{\partial \Gamma(x)}{\partial x} 2y \exp\left(-\frac{y^2}{2}\right) \tag{46c}$$

Table II. CPU time in seconds for obtaining a fixed relative error of the H-component (using a single 2 GHz Pentium IV processor).

Relative error (%)	Integration time	$P=2$		$P=4$		$P=6$	
		CPU	N	CPU	N	CPU	N
10	10	1.1E+00	144	3.7E−01	36	3.3E-01	16
	100	5.2E+01	400	1.0E+01	64	1.3E+01	36
1	10	3.2E+01	1296	2.1E+00	100	1.3E+00	36
	100	4.5E+02	1600	6.0E+01	196	3.1E+01	64

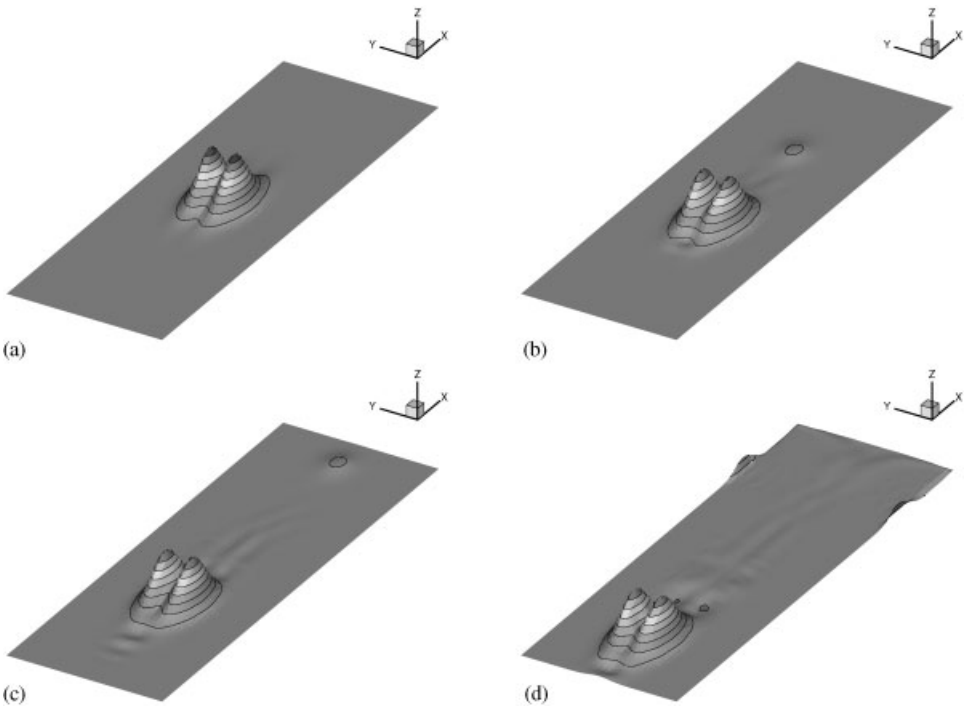

Figure 7. Propagation of an equatorial Rossby solitary wave: (a) Initial surface elevation; (b) after 10 time units; (c) after 20 time units and (d) after 40 time units.

where $\Gamma(x) = 0.771\ a^2\ \mathrm{sech}^2(ax)$ and where a is the parameter determining the amplitude of the solitary wave (set to 0.395). We discretized the 48×16 unit basin into 96 elements of order 8 and integrate for 40 time units using 1000 time steps. All boundaries are treated as walls. Figure 7 shows the evolution of the wave. Initially, the wave lose some mass

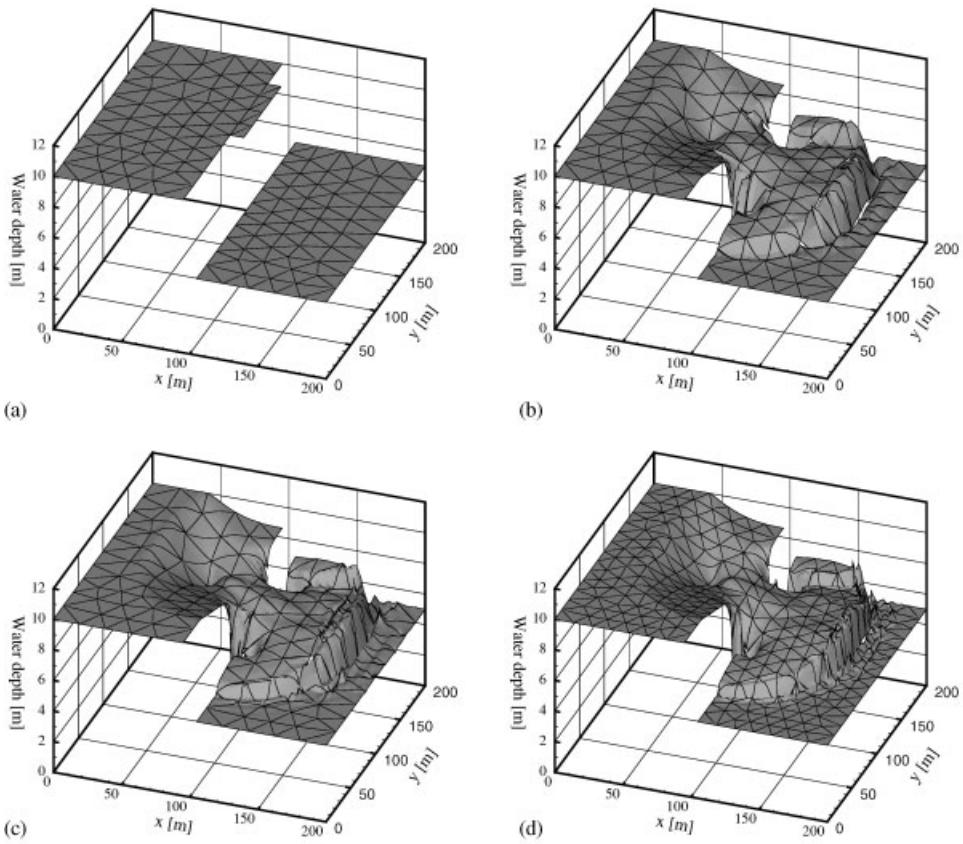

Figure 8. Dam-break problem. Non-limited solutions: (a) Initial state. Water depth at $t = 7.2$ s; (b) 214 elements of 4th order; (c) 214 elements of 6th order; and (d) 436 elements of 6th order.

as an eastward propagating Kelvin wave, which is caused by the use of non-exact initial condition [4]. The computed phase velocity is $-0.77\ \mathrm{m\ s^{-1}}$, in good agreement with the analytical value of $-0.78\ \mathrm{m\ s^{-1}}$. The result is in accordance with results obtained by high-order continuous Galerkin models [4, 5].

4.3. Dam-break

The instantaneous failure of an anti-symmetric dam is a standard test case for shock-capturing SWE models. The computational domain consists of a 200×200 m region with a 10 m wide dam. The dam runs parallel to the y-axis, centred at $x = 100$ m, while the breach is 75 m wide and centred at $y = 125$ m. The bottom is horizontal and frictionless. The water depth is 10 m upstream of the dam and 5 m downstream, see Figure 8(a). The fluid is initially at rest and at the upstream ($x = 0$ m) and downstream ($x = 200$ m) boundaries the water depth is held constant to the initial values. All other boundaries are treated as walls.

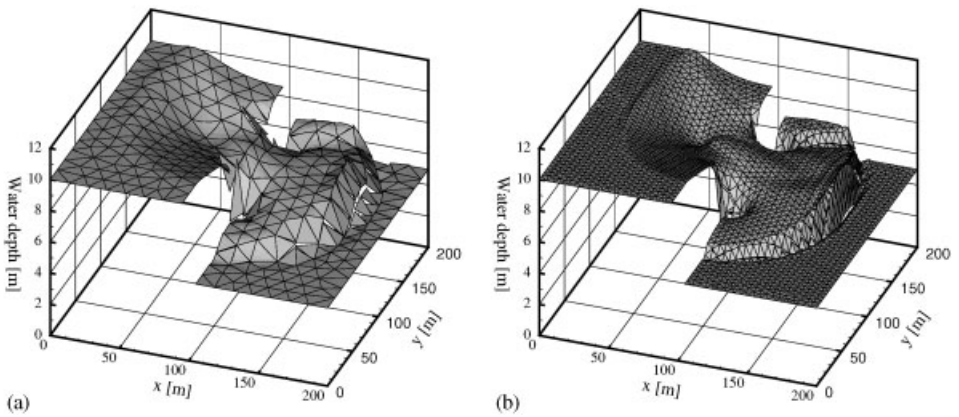

Figure 9. Dam-break problem: Limited solutions. Water depth at $t = 7.2$ s, (a) 436 elements of 3rd order; and (b) 3502 elements of 3rd order.

The domain is discretized into 214 elements and we simulate up to 7.2 s after the dam-break using a time step of 0.01 s. In Figure 8(b) and 8(c) we show the results using 4th- and 6th-order expansions without limiter, respectively. We observe a bore travelling downstream and a rarefaction wave travelling upstream. The results are, in general, similar to results presented in the literature [2, 23, 24] with the exception of the Gibbs oscillations inevitably produced by a high-order method without limiting. The solution is initially improved by the increase of polynomial order. However, after the solution is properly resolved the oscillations increase with increasing order, and no further benefit is obtained from p-type refinement. In addition, without any limiter the oscillations also increased when h-type refinement is performed, as seen from Figure 8(d). Nevertheless, the oscillations are confined to just the neighbouring elements and do not degrade the general solution away from the shock.

Figure 9 shows limited solutions of the same problem using 436 and 3502 elements of 3rd order. The limiter is invoked if the jump in water depth normalized with the mean water depth is larger than 0.01. We see that upstream of the dam the solution has not been limited to any larger extent in either of the two simulations. The shock transition takes in general two to three elements—which for the coarse mesh gives a very wide shock. A close look on Figure 9 reveals that there still are some minor oscillation present in both simulations, but on the whole the oscillations have been suppressed by the limiter.

4.4. Harbour problem

Here we illustrate the model's ability to handle complex geometries with the more practical application of wave disturbance in an harbour. Consider the realistic port layout presented in Figure 10. The layout is based on the Port of Visby, located on the island Gotland in the Baltic Sea, with the simplification that the break-waters are modelled to be fully reflective. During autumn storms waves with periods up to 9 s and heights over 4.5 m can attack the harbour from the direction indicated in Figure 10(a). As might be expected from the layout, problems are most severe at berth no. 5. The wave induced motions of the ferry usually moored at this berth can be so large it has to be moved to another berth in

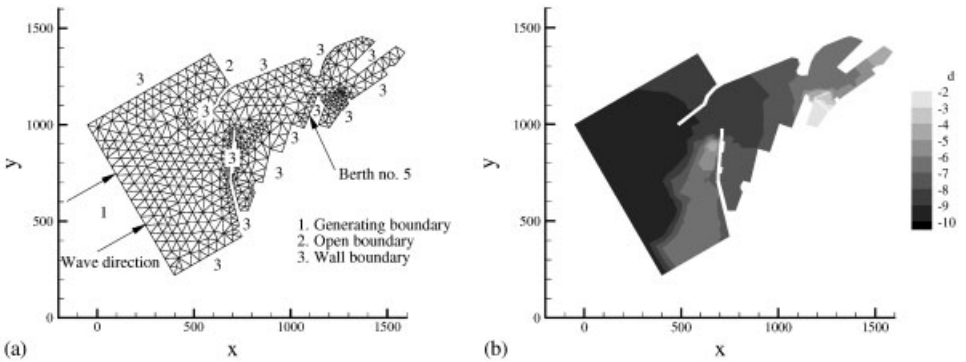

Figure 10. Harbour layout: (a) Mesh and boundary conditions, (b) depth.

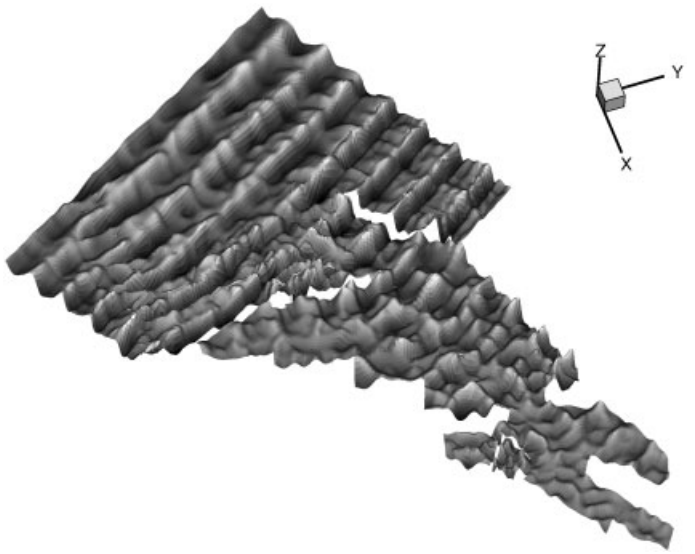

Figure 11. Snapshot of surface elevation after 500 s.

order to avoid damages on the RoRo ramps, causing disruption of the cargo handling in the port.

In this simulation, however, we illustrate the less severe case of a sinusoidal waves with a period of 10.1 s and heights of 0.5 m penetrates the harbour. For this case, we have applied a uniform bottom friction with a Manning number of $M = 0.031$. The water is initially assumed to be motionless. Figure 11 shows a snapshot of the surface elevation after running the model for 500 s using elements of polynomial order 5. At berth no. 5, the maximum wave height during the simulation is roughly 0.35 m. If the outer break-water is elongated with 200 m—as intended in the original layout, but abandoned for economic reasons—the wave height is decreased to approximately 0.25 m.

5. CONCLUSIONS

We have presented a high-order discontinuous Galerkin method for simulating 2D shallow water flows on unstructured triangular domains. The model employs orthogonal modal basis functions in space and a third-order Runge–Kutta scheme in time. The model was shown to exhibit optimal convergence, $\mathcal{O}(h^{P+1})$, for smooth problems. Thus, we obtain the expected exponential convergence in the case of p-type refinement, in accordance with previous continuous high-order Galerkin models [4, 5]. The exponential convergence, in combination with the diagonal mass matrix due to the orthogonal expansion basis, gives a computationally efficient model. The efficiency is seen to increase with increasing order of the model and time of integration—even for results of engineering accuracy.

The DG approach allows for discontinuous solutions, as illustrated with the dam-break test case, which lead to Gibbs oscillations in the absence of any artificial viscosity, filter or limiter. In contrast to classical continuous methods, however, the oscillations generally do not pollute the whole solution or cause 'blow-ups'. We removed the oscillations by applying the generalized slope limiter. As the slope limiter lower the approximation order to linear at the vicinity of a shock, it should ideally be combined with h-refinement to avoid losing accuracy upstream of the shock.

The model's geometrical flexibility and usefulness for 'real-life' applications was demonstrated considering wave disturbance in a harbour with complicated geometry. However, due to the non-dispersive properties of the SWE the restriction of the water depth to wave length ratio is too severe for many applications in coastal engineering. In order to relax the restriction and allow simulation of dispersive waves Boussinesq-type equations can be used, and present work is directed towards extending the SWE model to incorporate dispersive terms.

REFERENCES

1. Abbott MB. Computational hydraulics. *Elements of the Theory of Free Surface Flows*. Pitman: London, 1979.
2. Chaudry MH. *Open-Channel Flow*. Pretice-Hall: New Jersey, 1993.
3. Toro EF. *Shock-Capturing Methods for Free Surface Flows*. Wiley: Chichester, 2001.
4. Ma H. A spectral element basin model for the shallow water equations. *Journal of Computational Physics* 1993; **109**:133–149.
5. Iskandarani M, Haidvogel DB, Boyd JP. A staggered spectral element model with application to the oceanic shallow water equations. *International Journal for Numerical Methods in Fluids* 1995; **20**:393–414.
6. Cockburn B, Lin S-Y, Shu C-W. TVB Runge–Kutta local projection discontinuous Galerkin finite element method for conservation laws III: one-dimensional systems. *Journal of Computational Physics* 1989; **84**: 90–113.
7. Cockburn B, Shu C-W. TVB Runge–Kutta local projection discontinuous Galerkin finite element method for conservation laws V: multidimensional systems. *Journal of Computational Physics* 1998; **141**:199–224.
8. Cockburn B, Shu C-W. Runge–Kutta discontinuous Galerkin methods for convection-dominated problems. *Journal of Scientific Computing* 2001; **16**(3):173–261.
9. Biswas R, Devine KD, Flaherty JE. Parallel, adaptive finite element methods for conservation laws. *Applied Numerical Mathematics* 1994; **14**:255–283.
10. Burbeau P, Sagaut P, Bruneau Ch-H. A problem-independent limiter for high-order Runge–Kutta discontinuous Galerkin methods. *Journal of Computational Physics* 2001; **169**:111–150.
11. Lomtev I. A discontinuous Galerkin spectral/*hp* element method for compressible Navier–Stokes equations. *Ph.D. Thesis*, Brown University, 1998.
12. Schwanenberg D, Köngeter J. A discontinuous Galerkin method for the shallow water equations with source terms. In *Discontinuous Galerkin Methods*, Cockburn B, Karniadakis GE, Shu C-W (eds). Springer: Heidelberg, 2000; 289–309.
13. Li H, Liu RX. The discontinuous Galerkin finite element method for the 2d shallow water equations. *Mathematics and Computers in Simulation* 2001; **56**:171–184.

14. Aizinger V, Dawson C. A discontinuous Galerkin method for two-dimensional flow and transport in shallow water. *Advances in Water Resources* 2002; **25**:67–84.
15. Dupont, F. Comparison of numerical methods for modelling ocean circulation in basins with irregular coasts. *Ph.D. Thesis*, McGill University, 2001.
16. Giraldo FX, Hesthaven JS, Warburton T. Nodal high-order discontinuous Galerkin methods for the spherical shallow water equations. *Journal of Computational Physics* 2002; **181**:499–525.
17. Proriol J. Sur une famille de polynomes á deux variables orthogonaux dans un triangle. *Comptes Rendes de'l Academie des Sciences Paris* 1957; **257**:2459.
18. Koornwinder T. Two-variable analogues of the classical orthogonal polynomials. *Theory and Applications of Special Functions*. Academic Press: San Diego, 1975.
19. Dubiner M. Spectral methods on triangles and other domains. *Journal of Scientific Computing* 1991; **6**(4):345–390.
20. Karniadakis EmG, Sherwin SJ. *Spectral/hp Element Methods for CFD*. Oxford University Press: US, 1999.
21. Sanders BF. Non-reflecting boundary flux function for finite volume shallow-water models. *Advances in Water Resources* 2002; **25**:195–202.
22. Boyd JP. Equatorial solitary waves. Part I: Rossby solitons. *Journal of Physical Oceanography* 1980; **10**:1699–1717.
23. Wang J-W, Liu R-X. A comparative study of finite volume methods on unstructured meshes for simulation of 2D shallow water wave problems. *Mathematics and Computers in Simulation* 2000; **53**:171–184.
24. Zoppou C, Roberts S. Numerical solution of the two-dimensional unsteady dam break. *Applied Mathematical Modelling* 2000; **24**:457–475.

